ECS Solid State Letters, **1** (2) R9-R12 (2012)
2162-8742/2012/1(2)/R9/4/$28.00 © The Electrochemical Society

Photoluminescence Characteristics of In_2O_3 Quantum Dot (QD)-SiO_2 Nanocomposite Thin Films Containing Various QD Sizes

Yang-Ru Lyu and Tsung-Eong Hsieh[z]

Department of Materials Science and Engineering, National Chiao Tung University, Hsinchu 30010, Taiwan

Nanocomposite layers containing In_2O_3 quantum dots (QDs) with radii ranging from 1.8 to 5 nm embedded in SiO_2 matrix were prepared. Prominent blueshift with a drastic increase in emission efficiency for red, green and blue emissions were observed in the photoluminescence (PL) spectra of samples when QD radius was less than 1.32 nm. PL enhancement was further confirmed by the calibration of defect trap levels and indicated the Bohr radius of In_2O_3 QDs was 1.32 nm.
© 2012 The Electrochemical Society. [DOI: 10.1149/2.007202ssl] All rights reserved.

Manuscript submitted March 21, 2012; revised manuscript received May 11, 2012. Published July 20, 2012.

Quantized materials have attracted numerous interests in research and practical applications in past decade due to their unique physical and chemical properties. For instance, nanometer-scale semiconductors in various geometrical forms have been prepared and, with the presence of quantum confinement effects, their optoelectronic properties have been investigated in detail.[1–3] Indium oxide (In_2O_3) is one of the important wide-bandgap semiconductors with bandgap (E_g) = 3.75 eV (for direct bandgap) or 2.61 eV (for indirect bandgap)[4] and its applications to solar cells,[5] field-emission displays,[6] biosensors,[7] gas sensors,[8] optoelectronics,[9] and photocatalysis[10] have been demonstrated. In_2O_3 was often synthesized in one-dimensional forms, e.g., nanofibers[11] or nanowires (NWs),[12,13] so that the high surface-to-volume feature can be applied to fast response gas detection. For zero-dimensional nano-structure, the In_2O_3 in nanoparticle form is relatively difficult to obtain although various physical and chemical processing methods such as thermal evaporation, sputtering, ion plating, oxygen ion assisted deposition, sol-gel methods and laser ablation deposition[14–19] have been employed. This consequently impoverishes the fundamental understanding on In_2O_3 quantum dots (QDs). For instance, the Bohr radius, a key parameter essential to the quantum confinement effects of nanostructures, of In_2O_3 QDs remains in debate. Calibration based on the study of In_2O_3 nanofibers indicated that the critical Bohr radius is about 2.14 nm.[11] Zhou et al. reported the exciton Bohr radius for In_2O_3 nanoparticle is in the range of 1.3 and 2.5 nm.[20] Yin et al. also reported the Bohr radius of In_2O_3 nanorods, nanoellipses, microspheres, and microbricks are about 11.4 nm.[21] Discrepancies in Bohr radius of In_2O_3 QDs reported by theoretical calculations might result from adopting the parameters of bulk materials for calculations.[11] In experimental studies, the Bohr radius of In_2O_3 QDs was usually determined in terms of the blueshift phenomena of band edge. Nevertheless, the sample purities and data handling methods might interrupt the band edge judgment.[22,23] Hence, further study is required to clarify the exact value of Bohr radius of In_2O_3 QDs. In this study, nanocomposite thin films containing In_2O_3 QDs of various sizes embedded in SiO_2 matrix are prepared and their photoluminescence (PL) properties are characterized. In addition to the microstructures, the PL efficiencies and the defect trap levels of samples are calibrated so as to identify the Bohr radius of In_2O_3 QDs.

Experimental

Target-attachment sputtering method[24] was adopted to prepare the nanocomposite thin films containing In_2O_3 QDs embedded in SiO_2 matrix. First, high-purity In_2O_3 (99.99%) powder supplied by CERAC/USA was pressed in the pellet form with 12 mm in diameter. Various amounts of In_2O_3 pellets were then mounted on a 3-inch quartz target for sputtering deposition in a vacuum system with background pressure better then 10^{-7} torr. Without intentional substrate heating, the sample deposition was carried out at working pressure of 3.5 mtorr and RF sputtering power of 70–160 W with argon (Ar) as the inlet gas flow. The surface-area-coverage ratios of In_2O_3 pellets on quartz target were adjusted in a range of 5 to 35% in order to modulate the contents of In_2O_3 QDs in the nanocomposite samples. Notably, part of the In_2O_3 pellets were subjected to a sintering at 1100°C and adopted for sample preparation. The sintered In_2O_3 pellets possessed a lower sputtering yield so that the ultra-small-size In_2O_3 QDs could be achieved. This allowed the preparation of nanocomposite samples containing QDs with a relatively wide size range. Sample designation and the preparation conditions are listed in Table I. The thickness of thin-film samples was fixed at about 600 nm to avoid the bias on physical property comparison.

Relevant characterizations were performed immediately after the completion of sputtering deposition without performing the post annealing treatment. Microstructures and compositions of nanocomposite layers were separately examined by a field-emission transmission electron microscope (FE-TEM; JEOL JEM-2100F) operating at 200 kV and an X-ray photoemission spectroscopy (XPS; American Physical Electronics ESCA PHI 1600) using Mg K_α excitation. PL spectra of samples were measured at room temperature by using a self-assembly PL apparatus within a 325-nm He-Cd laser at fixed beam size of 1.2 mm and a HORIBA Jobin Yvon iHR-320 spectrometer at the resolution of 0.03 nm (calibrated at 546.07 nm using a 2400 gr/mm grating).

Results and Discussion

Figures 1a–1g present the TEM micrographs of In_2O_3 QD-SiO_2 nanocomposite films for samples *a* to *g*. Discrete In_2O_3 QDs uniformly dispersed in SiO_2 matrix can be seen in all samples except samples *d* and *e* which exhibit severe overlapping and coalescence of QDs due to the excessive usage of In_2O_3 pellets. Note that the quantized effects of In_2O_3 QDs in samples *d* and *e* were diminished accordingly as illustrated by the PL property presented below. The average sizes of QDs (radius in nm) in various samples were obtained by measuring at least 60 In_2O_3 QDs in the TEM images and the results are listed in Table I. For the samples prepared at the same amount of In_2O_3 pellets but various RF powers, e.g., samples *a*, *b* and *c*, the QD size decreases with the decrease of sputtering power. A similar result was also observed in samples *f* and *g*. However, the influence of sputtering power on QD size was found to be moderate. A comparison of QD sizes of samples prepared using a sole In_2O_3 pellet (samples *a*, *b*, *c*, *f* and *g*) indicated the pellet sintering is essential to a substantial reduction of QD size. The 1100°C-sintering effectively increased the density of In_2O_3 pellet and suppressed its sputtering yield, consequently resulting in the reduction of In_2O_3 QD size and content in the samples. By taking the advantage of this feature and, in conjunction with the modulation of sputtering power, we were able to prepare the In_2O_3 QDs with the radii in a relatively wide range of 1.8 to 5.0 nm. Table I also lists the volume ratios of In_2O_3 QDs in nanocomposite layers deduced by XPS analysis. It can be seen that the number of In_2O_3

[z]E-mail: tehsieh@mail.nctu.edu.tw

Downloaded on 2014-04-28 to IP 140.113.38.11 address. Redistribution subject to ECS terms of use (see ecsdl.org/site/terms_use) unless CC License in place (see abstract).

Table I. A summary of sample designation, In_2O_3 contents, QD sizes, and PL emission locations of In_2O_3 QD-SiO_2 nanocomposite samples.

Sample designation	Sputtering condition		QD radius (nm)	In_2O_3content (Vol.%)	Emission peak position (nm)		
	RF power (W)	Pellet No.			Red	Green	Blue
a	160	1	5.0	12.5	648	572	510
b	130	1	4.8	11.9	642	566	504
c	100	1	4.4	11.4	632	564	492
d[a]	130	5	4.1	74.1	627	559	487
e[a]	130	3	2.6	27.9	602	524	446
f[a]	130	1	2.2	7.2	586	501	419
g[a]	70	1	1.8	6.7	564	481	399

[a]Prepared by using the sintered In_2O_3 pellets.

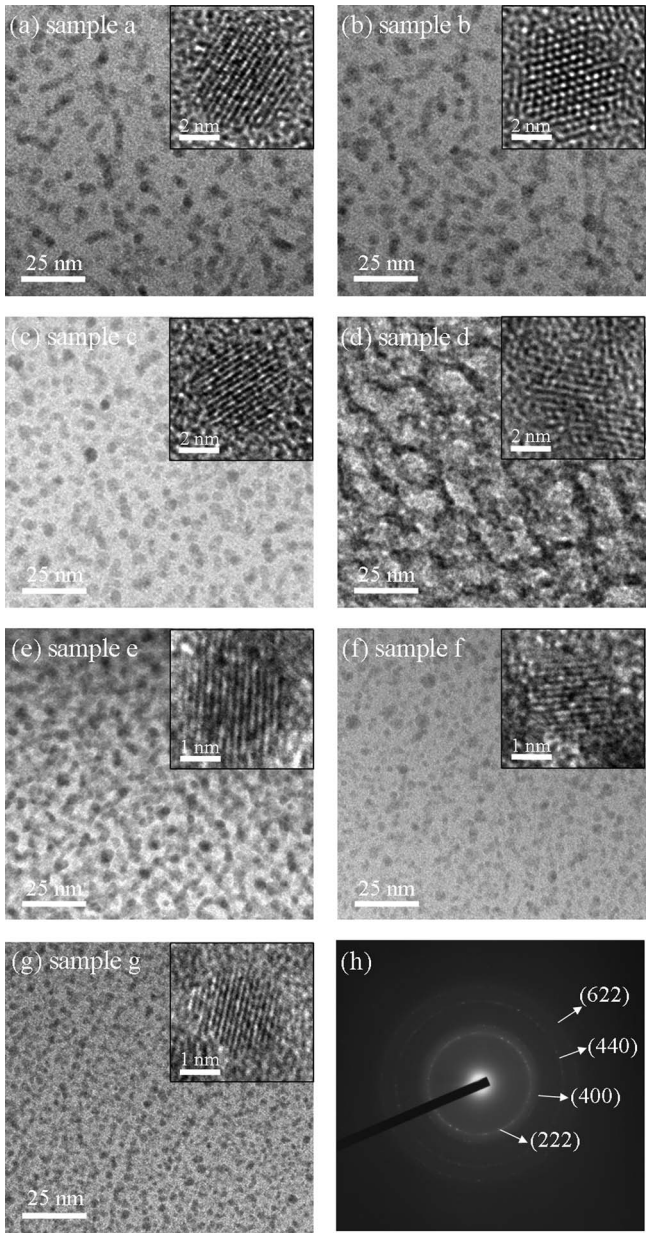

Figure 1. TEM images of samples *a-g* are shown in (a)-(g). The insets at upper right-hand corner of each micrograph are the high-magnification images of In_2O_3 QDs. Typical SAED pattern of In_2O_3 QD-SiO_2 nanocomposite samples is given in (h) and is indexed in accord with the JCPDS standard.

pellets adopted for sputtering mainly affects the In_2O_3 content of the sample as indicated by the In_2O_3 volume ratios of samples *d*, *e* and *f*. Though pellet number might also affect the QD size, it is believed that the coarse QDs in the samples prepared by using large amount of In_2O_3 pellets is correlated to the particle overlapping/coalescence as illustrated by the microstructures of samples *d* and *e* depicted in Figs. 1d and 1e.

The insets at the upper right-hand corner of Figs. 1a–1g are the enlarged images of In_2O_3 QDs in various samples. Lattice fringes presenting in the QDs indicate each of the QDs corresponds to a single crystalline particle, a feature that would greatly benefit the optoelectronic performance of such a hybrid thin films. Representative selected area electron diffraction (SAED) pattern of In_2O_3 QD-SiO_2 nanocomposite samples is shown in Fig. 1h. With the aid of the Joint Committee of Powder Diffraction Standard (JCPDS) file No. 06-0416, the In_2O_3 QDs were identified as the body-centered-cubic (BCC) phase with space-group symbol $\mathbf{Ia}_3$.

Figure 2 depicts the PL spectra and the de-convoluted profiles of In_2O_3 QD-SiO_2 nanocomposite samples obtained by Gaussian curve fitting method.[25] For the samples *a-c* prepared within the non-sintered In_2O_3 pellets, the emission spectra locate mainly at the wavelength range of 400 to 750 nm with a moderate difference in profile shape. On the contrary, dramatic differences in emission intensity and profile shape were observed in samples *d-g* prepared by using the sintered In_2O_3 pellets. Moreover, the samples with severe QD overlapping/coalescence, e.g., samples *d* and *e*, exhibit insignificant PL intensities in comparison with samples *f* and *g* containing uniformly dispersed, discrete In_2O_3 QDs. In particular, emission intensities are drastically enhanced for samples *f* and *g*, revealing the interfacial and quantized effects contributed by the embedment of sufficiently small In_2O_3 QDs in such samples.

As illustrated by the curving fitting results of PL spectra shown in Fig. 2, all spectra could be de-convoluted into red, green and blue emission bands. The corresponding emission peak positions summarized in Table I indicate, as the QD size decreases, all emissions shift toward the short wavelength side. As indicated by the plots of peak positions and integrated intensities of emission bands against the QD radius shown in Figs. 3a and 3b, the blueshift and emission efficiencies become pronounced when the QD radius is less than 1.32 nm. Such a phenomenon was ascribed to the quantum confinement effect since the strong confinement emerged when the QD radius is less than the Bohr radius. Notably, the Bohr radius deduced from the PL analysis is about equal to the low bound value of Bohr radii in a range of 1.3 to 11.4 nm reported by previous studies.[11,20,21] This is further validated by the calibration of defect trap levels presented as follows.

Assume the PL properties of samples are correlated with the transitions of electrons from conduction band edge (E_c) to the defect trap levels in In_2O_3 QDs. The energetic position of the defect trap level in an In_2O_3 QD can thus be expressed as

$$E_{trap} = E_c - E_{emission} \quad (1)$$

Downloaded on 2014-04-28 to IP 140.113.38.11 address. Redistribution subject to ECS terms of use (see ecsdl.org/site/terms_use) unless CC License in place (see abstract).

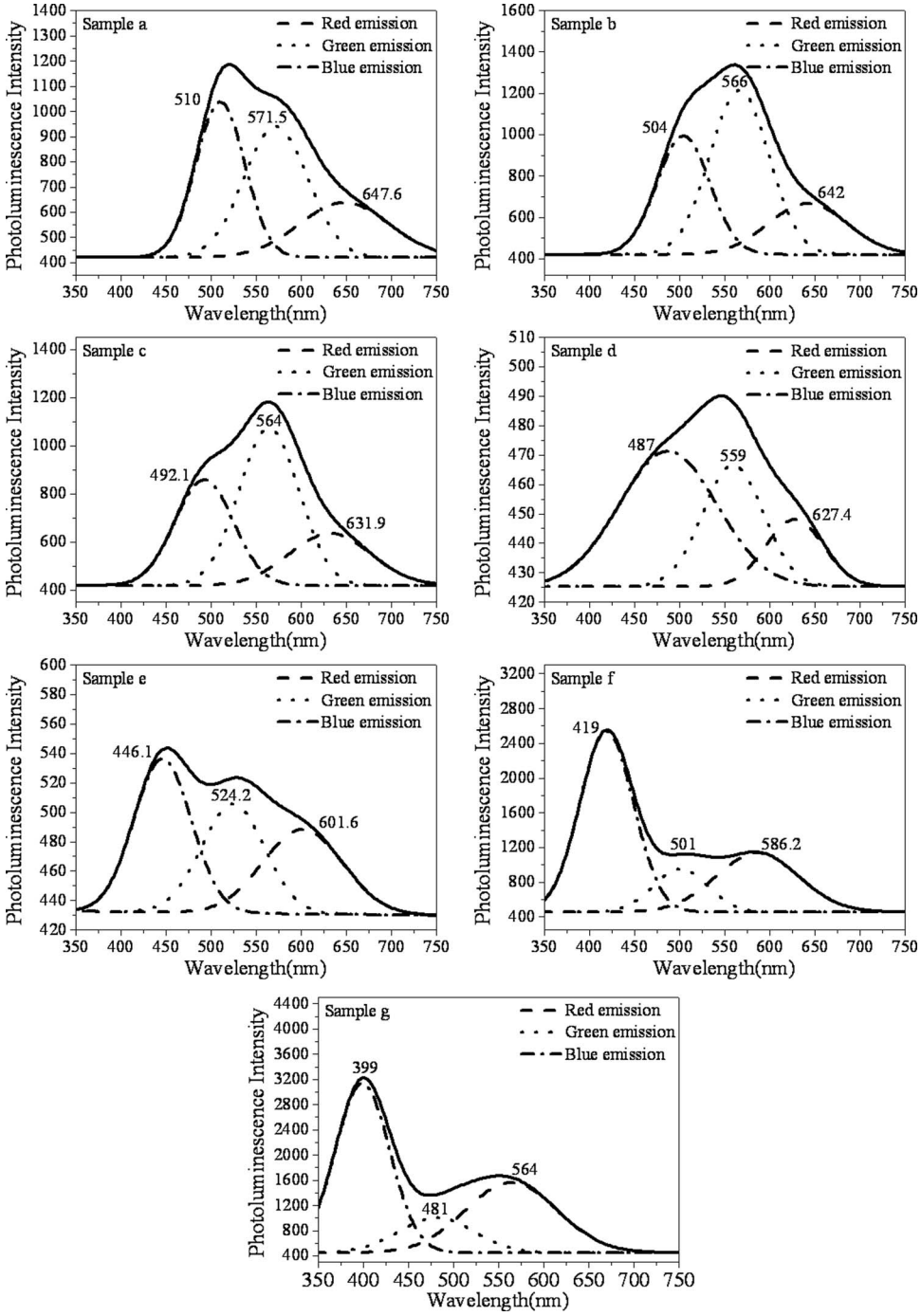

Figure 2. Curve fitting results for PL spectra for In_2O_3 QD-SiO_2 nanocomposite samples *a-g*.

where E_{trap} is the energetic position of the defect trap level and $E_{emission}$ is the photon energy of the emission band. The E_c and edge of the valence band (E_v) can be also expressed as functions of the QD radius in terms of the Brus' model:[26,27]

$$E_c = E_g + \frac{h^2}{8m_e^* r^2} - \frac{0.9e^2}{4\pi\varepsilon_0\varepsilon_\infty r} \quad (2)$$

and

$$E_v = \frac{h^2}{8m_h^* r^2} - \frac{0.9e^2}{4\pi\varepsilon_0\varepsilon_\infty r} \quad (3)$$

where E_g for the bulk In_2O_3 is 3.75 eV, r is the QD radius, m_e^* is the effective mass of electron (=0.35 m_o), m_h^* is the effective mass of hole (= 0.6 m_o) and ε_∞ is the high-frequency dielectric constant for In_2O_3 (=7).[24] By plugging the QD sizes and PL data listed in Table I into Eqs. (1)–(3), one is able to plot the defect trap levels and their energetic positions in the bandgap of In_2O_3 against the QD radius as depicted in Fig. 3c. An obvious shift of trap levels occurs when QD radius is less than 1.32 nm, in agreement with the finding of PL properties. The Bohr radius of In_2O_3 QDs was hence identified the as 1.32 nm.

Conclusions

In conclusion, the nanocomposite samples containing In_2O_3 QDs with sizes ranging from 1.8 to 5 nm embedded in SiO_2 matrix were prepared by utilizing the target-attachment sputtering method. TEM analysis revealed the In_2O_3 QDs are single crystalline with BCC structure. The PL spectra of In_2O_3 QD-SiO_2 nanocomposite layers

Downloaded on 2014-04-28 to IP 140.113.38.11 address. Redistribution subject to ECS terms of use (see ecsdl.org/site/terms_use) unless CC License in place (see abstract).

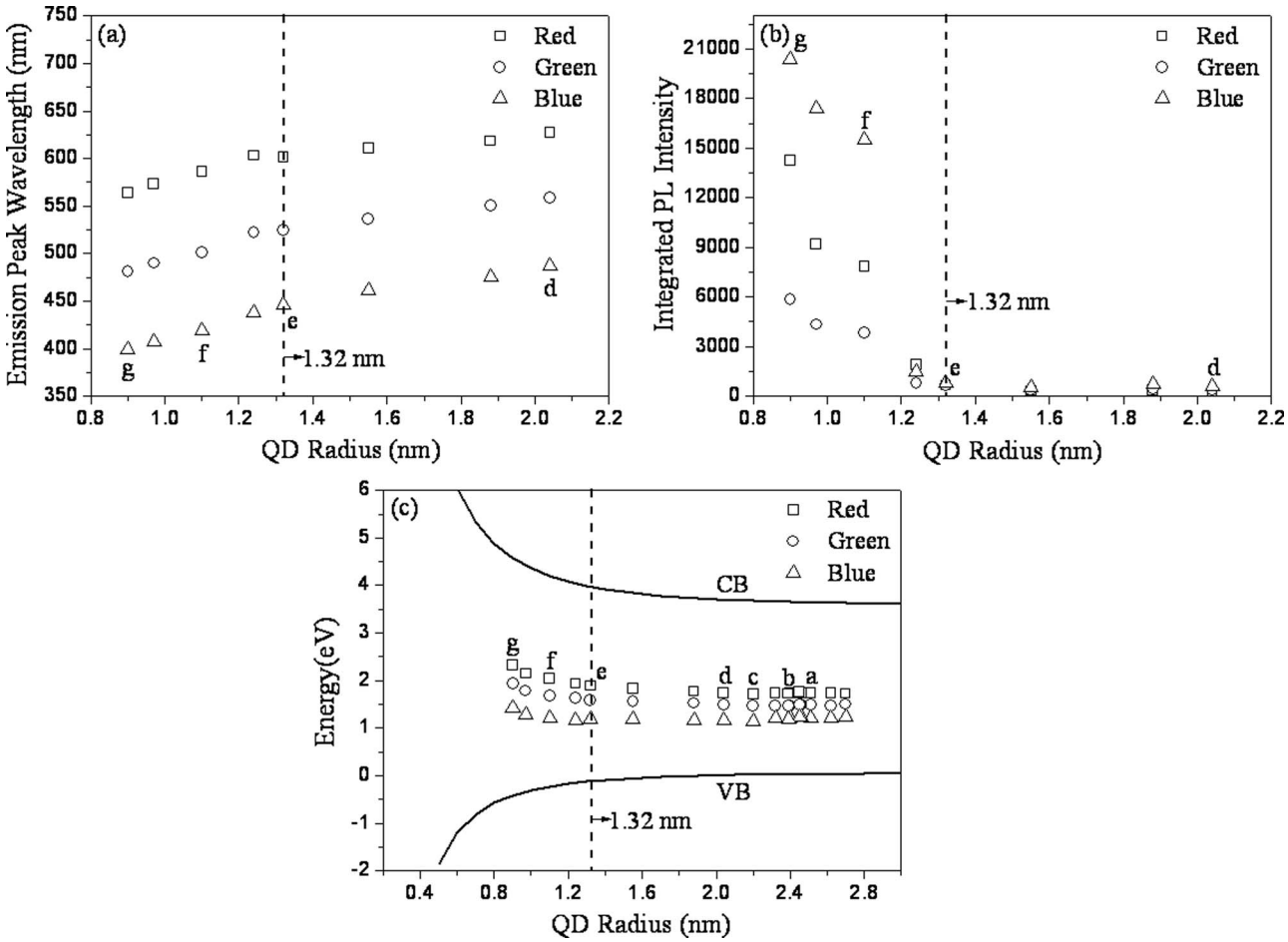

Figure 3. (a) Peak position and (b) integrated intensity of red, green and blue emissions deduced from the de-convoluted PL spectra of In_2O_3 QD-SiO_2 nanocomposite samples as a function of QD radius. (c) The energetic positions of defect trap levels of In_2O_3 QDs *versus* the QD radius calibrated in term of the Brus' model. The red, green and blue emissions correspond to the transitions either from E_c to a specific E_{trap} or from a specific E_{trap} to E_v as defined in Eqs. (1)–(3). The letters *a-b* in above figures denoted the designation of samples prepared in this work.

were found to comprise of the red, green and blue emissions and the emission peaks shift toward the shorter wavelength side when the QD size is decreased. Moreover, the blueshift became pronounced when the QD radius was smaller than 1.32 nm, implying the occurrence of strong confinement effects in the samples containing QDs with radii less than such a value. The blueshift phenomenon was found in good agreement with the plot of integrated PL intensities for the three emissions and the calibration of defect trap levels against the QD radius, which allowed the identification of the Bohr radius of In_2O_3 QDs as 1.32 nm.

Acknowledgments

This work is supported by National Science Council (NSC), Taiwan, R.O.C., under the contract No. NSC100-2221-E-009-054-MY2. Assistance of TEM analysis provided by Dr. Wei-Lin Wang and Dr. Li Chang at Department of Materials Science and Engineering, National Chiao Tung University, Taiwan, R.O.C., is also deeply acknowledged.

References

1. X. H. Zhang, S. J. Chua, A. M. Yong, S. Y. Chow, H. Y. Yang, S. P. Lau, and S. F. Yu, *Appl. Phys. Lett.*, **88**, 221903 (2006).
2. B. Damilano, N. Grandjean, F. Semond, J. Massies, and M. Leroux, *Appl. Phys. Lett.*, **75**, 962 (1999).
3. J. Lee, V. C. Sundar, J. R. Heine, M. G. Bawendi, and K. F. Jensen, *Adv. Mater.*, **12**, 1102 (2000).
4. R. L. Weiher and R. P. Ley, *J. Appl. Phys.*, **37**, 299 (1966).
5. Z. B. Zhou, R. Q. Cui, Q. J. Pang, Y. D. Wang, F. Y. Meng, T. T. Sun, Z. M. Ding, and X. B. Yu, *Appl. Surf. Sci.*, **172**, 245 (2001).
6. Y. X. Liang, S. Q. Li, L. Nie, Y. G. Wang, and T. H. Wang, *Appl. Phys. Lett.*, **88**, 193119 (2006).
7. M. Curreli, C. Li, Y. H. Sun, B. Lei, M. A. Gundersen, M. E. Thompson, and C. W. Zhou, *J. Am. Chem. Soc.*, **127**, 6922 (2005).
8. T. Hibino, S. Tanimoto, S. Kakimoto, and M. Sanob, *Electrochem. Solid-State Lett.*, **2**, 651 (1999).
9. C. Y. Kuo, S. Y. Lu, and T. Y. Wei, *J. Cryst. Growth*, **285**, 400 (2005).
10. B. Li, Y. Xie, M. Jing, G. Rong, Y. Tang, and G. Zhang, *Langmuir*, **22**, 9380 (2006).
11. C. H. Liang, G. W. Meng, Y. Lei, F. Phillipp, and L. D. Zhang, *Adv. Mater.*, **13**, 1330 (2001).
12. X. C. Wu, J. M. Hong, Z. J. Han, and Y. R. Tao, *Chem. Phys. Lett.*, **373**, 28 (2003).
13. M. Mazzera, M. Zha, D. Calestani, A. Zappettini, L. Lazzarini, G. Salviati, and L. Zanotti, *Nanotechnology*, **18**, 355707 (2007).
14. Y. Shigesato and D. C. Paine, *Thin Solid Films*, **238**, 44 (1994).
15. H. Kobayashi, T. Ishida, K. Nakamura, Y. Nakato, and H. Tsubomura, *J. Appl. Phys.*, **72**, 5288 (1992).
16. M. Higuchi, M. Sawada, and Y. Kuronuma, *J. Electrochem. Soc.*, **140**, 1773 (1993).
17. J. S. Cho, K. H. Yoon, and S. K. Koh, *J. Appl. Phys.*, **89**, 3223 (2001).
18. R. B. H. Tahar, T. Ban, Y. Ohya, and Y. Takahashi, *J. Appl. Phys.*, **82**, 865 (1997).
19. A. Murali, A. Barve, V. J. Leppert, S. H. Risbud, I. M. Kennedy, and H. W. H. Lee, *Nano Letters*, **1**, 287 (2001).
20. H. J. Zhou, W. P. Cai, and L. D. Zhang, *Appl. Phys. Lett.*, **75**, 495 (1999).
21. W. Yin, D. V. Esposito, S. Yang, C. Ni, J. G. Chen, G. Zhao, Z. Zhang, C. Hu, M. Cao, and B. Wei, *J. Phys. Chem. C*, **114**, 13234 (2010).
22. S. Das, S. Chakrabarti, and S. Chaudhuri, *J. Phys. D: Appl. Phys.*, 4021 (2005).
23. M. G. Panthani, V. Akhavan, B. Goodfellow, J. P. Schmidtke, L. Dunn, A. Dodabalapur, P. F. Barbara, and B. A. Korgel, *J. AM. CHEM. SOC.*, **130**, 16770 (2008).
24. Y. Y. Peng and T.-E. Hsieh, *Appl. Phys. Lett.*, **89**, 211909 (2006).
25. J. H. Noggle, Practical curve fitting and data analysis: software and self-instruction for scientists and engineers, Ellis Horwood, Hemel Hempstead (1993).
26. L. E. Brus, *J. Phys. Chem.*, **90**, 2555 (1986).
27. A. van Dijken, E. A. Meulenkamp, D. Vanmaekelbergh, and A. Meijerink, *J. Lumin.*, **90**, 123 (2000).

Downloaded on 2014-04-28 to IP 140.113.38.11 address. Redistribution subject to ECS terms of use (see ecsdl.org/site/terms_use) unless CC License in place (see abstract).